RAPID COMMUNICATION

Bismuth doping enhanced tunability of strain-controlled magnetic anisotropy in epitaxial $Y_3Fe_5O_{12}$(111) films

Yunpeng Jia(贾云鹏)[1], Zhengguo Liang(梁正国)[1], Haolin Pan(潘昊霖)[1], Qing Wang(王庆)[1], Qiming Lv(吕崎鸣)[1], Yifei Yan(严轶非)[2], Feng Jin(金锋)[1], Dazhi Hou(侯达之)[1,2], Lingfei Wang(王凌飞)[1,2,†], and Wenbin Wu(吴文彬)[1,2,3,‡]

[1] *Hefei National Research Center for Physical Sciences at the Microscale, University of Science and Technology of China, Hefei* 230026, *China*

[2] *Department of Physics, University of Science and Technology of China, Hefei* 230026, *China*

[3] *Anhui Key Laboratory of Condensed Matter Physics at Extreme Conditions, High Magnetic Field Laboratory, HFIPS, Anhui, Chinese Academy of Sciences, Hefei* 230031, *China*

(Received 28 March 2022; revised manuscript received 13 April 2022; accepted manuscript online 18 April 2022)

$Y_3Fe_5O_{12}$ (YIG) and $BiY_2Fe_5O_{12}$ (Bi:YIG) films were epitaxially grown on a series of (111)-oriented garnet substrates using pulsed laser deposition. Structural and ferromagnetic resonance characterizations demonstrated the high epitaxial quality, extremely low magnetic loss and coherent strain state in these films. Using these epitaxial films as model systems, we systematically investigated the evolution of magnetic anisotropy (MA) with epitaxial strain and chemical doping. For both the YIG and Bi:YIG films, the compressive strain tends to align the magnetic moment in the film plane while the tensile strain can compete with the demagnetization effect and stabilize perpendicular MA. We found that the strain-induced lattice elongation/compression along the out-of-plane [111] axis is the key parameter that determines the MA. More importantly, the strain-induced tunability of MA can be enhanced significantly by Bi doping; meanwhile, the ultralow damping feature persists. We clarified that the cooperation between strain and chemical doping could realize an effective control of MA in garnet-type ferrites, which is essential for spintronic applications.

Keywords: yttrium iron garnet, strain engineering, doping, magnetic anisotropy

PACS: 75.30.Gw, 75.50.Gg, 75.47.Lx, 75.75.–c **DOI:** 10.1088/1674-1056/ac67cc

1. Introduction

The garnet-type ferrite yttrium iron garnet ($Y_3Fe_5O_{12}$, YIG), a ferrimagnetic insulator, has attracted extensive research interest for decades due to its ultralow Gilbert damping constant.[1,2] Such a low damping constant allows a long spin-wave propagation length up to a millimeter scale.[3] Moreover, its insulating feature eliminates charge flow and thus facilitates the generation of pure spin current.[4,5] Thanks to these superior properties, YIG films are considered an ideal platform for spintronic research and spintronic devices with low energy consumption.[2,6,7] Numerous works have demonstrated the important role of YIG in various spintronic phenomena, including spin-transfer torque, the (inverse) spin Hall effect, spin Hall magnetoresistance (SMR), spin pumping and the spin Seebeck effect.[8–14]

The spin transport properties of YIG-based functional devices strongly rely on the controllability of the orientation of the magnetic moment. For example, the SMR can reach the lowest value as the magnetic moments align in the YIG film plane and perpendicular to the charge current in the Pt capping layer.[11] Perpendicular magnetic anisotropy (PMA) is believed to provide better thermal stability and lower power consumption for spintronic devices.[15] Therefore, similar to other spintronic systems, harnessing the magnetic anisotropy (MA) of YIG films is one of the central challenges for this system.[16–18] Note that the magnetoelastic coefficient of the (111)-oriented rare earth iron garnet film is negative.[19,20] This feature makes the epitaxial strain imposed from the single crystal substrate an effective route for controlling the MA of the YIG films.[19] For example, PMA can be realized by growing the YIG films on garnet substrates with a larger lattice constant, such as $Gd_{2.6}Ca_{0.4}Ga_{4.1}Mg_{0.25}Zr_{0.65}O_{12}$,[21] $Gd_3Sc_2Ga_3O_{12}$[22] or $Gd_{0.63}Y_{2.37}Sc_2Ga_3O_{12}$.[23] Recently, it has been reported that chemical doping can also effectively modulate the MA of YIG films: dopants include Bi,[24,25] Mn,[26,27] and Ce.[28] However, both experimental routes have shortcomings. On one hand, large lattice mismatches between the films and substrates usually cause considerable strain relaxation, which degrades the tunability of MA. On the other hand, chemical doping inevitably causes disorder and defects in the films, which may increase magnetic loss. Moreover, the cooperative effects of doping and epitaxial strain on MA have rarely been investigated.

In this work, we chose (111)-oriented high-quality YIG and Bi-doped YIG ($BiY_2Fe_5O_{12}$, Bi:YIG) epitaxial films as model systems and performed a comparative study on the effects of strain and doping on MA. The YIG and Bi:YIG films were grown on a variety of garnet substrates with different lat-

†Corresponding author. E-mail: wanglf@ustc.edu.cn

‡Corresponding author. E-mail: wuwb@ustc.edu.cn

© 2023 Chinese Physical Society and IOP Publishing Ltd

tice constants. Thanks to the high epitaxial quality, all the YIG and Bi:YIG films with different thicknesses were coherently strained to the substrates. Accordingly, we could systematically characterize the evolution of MA with epitaxial strain. We found that the rhombohedral distortion of the film lattice along the out-of-plane (111) axis is the key parameter that determines the MA of both YIG and Bi:YIG films. More importantly, we found that the strain-induced tunability of MA can be enhanced significantly by Bi doping, while the ultra-low magnetic loss feature persists. Our work provides important guidelines for achieving effective control of MA in garnet-type ferrite-based thin films and heterostructures, which may promote these material systems for practical spintronic applications.

2. Method and materials

The YIG and Bi:YIG ceramic targets were prepared by traditional solid-state reactions. The original compounds, i.e., Y_2O_3, Fe_2O_3 and Bi_2O_3 powder, were mixed according to the stoichiometry and then calcined sequentially at 750 °C and 920 °C for 12 h. After being pressed into a YIG (Bi:YIG) pellet with a diameter of 1 inch at 30 MPa, the targets were sintered at 1300 °C (1100 °C) for 12 h (5 h).

We grew all the YIG and Bi:YIG ($BiY_2Fe_5O_{12}$) epitaxial films of thickness 10 nm, 30 nm, and 60 nm via pulsed laser deposition (PLD) on a variety of (111)-oriented garnet substrates. During deposition, we kept the substrate temperature at 730 °C. For YIG film growth we set the oxygen partial pressure and laser fluence as 4 Pa and 3.40 J·cm^{-2}. For growth of the Bi:YIG films we increased the oxygen partial pressure to 12 Pa and decreased the laser fluence to 1.63 J·cm^{-2} with the aim of suppressing the volatility of Bi. After deposition, the films were annealed *in situ* for 15 min to prevent the formation of oxygen vacancies. The film thickness was controlled by counting the number of laser pulses.

The epitaxial quality of the YIG and Bi:YIG films was analyzed by high-resolution x-ray diffraction (XRD; PANalytical, Empyrean). The film surface morphologies were characterized by atomic force microscopy (AFM; Asylum Research, MFP-3D) in contact mode. To characterize the magnetic properties we utilized a custom-built electromagnet to perform ferromagnetic resonance (FMR) measurements and a vibrating sample magnetometer (SQUID-VSM, Quantum Design) to measure the static magnetization at 300 K.

3. Results and discussion

To impose different epitaxial strain states on the YIG and Bi:YIG films, we chose to grow the films on a variety of (111)-oriented garnet substrates, including $Gd_3Ga_5O_{12}$ (GGG), $Y_3Sc_2Ga_3O_{12}$ (YSGG), $Gd_{2.6}Ca_{0.4}Ga_{4.1}Mg_{0.25}Zr_{0.65}O_{12}$ (SGGG), $Gd_{0.63}Y_{2.37}Sc_2Ga_3O_{12}$ (GYSGG), and $Gd_3Sc_2Ga_3O_{12}$ (GSGG). Bulk YIG, Bi:YIG, GGG, and other garnet substrates share a similar cubic unit cell. Figure 1(a) schematically displays the detailed crystal structure of YIG and GGG. In the cubic unit cell of YIG, 40% of Fe^{3+} ions occupy the A-site and form octahedra with six adjacent oxygen ions while 60% of Fe^{3+} ions occupy the D-site and form tetrahedra with four adjacent oxygen ions. The Y^{3+} ions occupy the C-site and form dodecahedra with eight adjacent oxygen ions.[29] The similar atomic structures of GGG, other garnet substrates and YIG enables a coherent heteroepitaxy. The lattice constants of bulk YIG, bulk Bi:YIG and various garnet substrates (a_{sub}) are summarized in Table 1. We also include the lattice mismatches between films and substrates (ε) in Table 1. Positive (negative) ε values represent in-plane tensile (compressive) strain states imposed by the substrates. For these (111)-oriented films, such a tensile (compressive) strain is expected to shorten (elongate) the film lattice along the out-of-plane [111] axis.

Table 1. Lattice mismatch (ε) of YIG and Bi:YIG with GGG, YSGG, SGGG, GYSGG, and GSGG(111) substrates.

Substrate	Lattice constant (Å)	Lattice mismatch with YIG (%)	Lattice mismatch with Bi:YIG (%)
YIG	12.376	–	–
Bi:YIG	12.406	–	–
GGG	12.376	0	−0.238
YSGG	12.426	0.404	0.165
SGGG	12.48	0.840	0.600
GYSGG	12.507	1.059	0.818
GSGG	12.554	1.438	1.197

We first check the epitaxial structure of YIG and Bi:YIG films via XRD. Figures 1(b) and 1(d) show the 2θ–ω XRD linear scans of the YIG and Bi:YIG epitaxial films near (444) diffraction. All the curves exhibit well-defined (444) diffraction peaks and Laue fringes, demonstrating the high epitaxial quality and sharp film–substrate interfaces. The 2θ–ε curve is summarized in Fig. S1 in the supplementary materials. As a_{sub} increases, the (444) diffraction peak of both YIG and Bi:YIG gradually shifts to a higher angle (indicated by the dashed lines in Figs. 1(b) and 1(d)), which signifies a gradually decreased (111) plane distance $d_{(111)}$. Note that the cation radius of Bi^{3+} is larger than that of Y^{3+},[21] which makes the lattice constant of Bi:YIG slightly larger than that of YIG. As a result, given the same substrate, the (444) peak of Bi:YIG always appears at a lower angle than that of YIG. Figures 1(c) and 1(e) show the normalized rocking curves of the YIG and Bi:YIG (444) peaks. All the curves show narrow and symmetrical peaks without any broad backgrounds. The full width at half maximum (FWHM) of these rocking curves is summarized in Table S1. All the values are below 0.02°, manifesting a superior high crystallinity. The surface morphology

of 30 nm thick YIG and Bi:YIG films was checked using the AFM images (Fig. S2 in the supplementary materials). The root-mean-square roughness of both YIG and Bi:YIG films is below 0.1 nm, consistent with the XRD results.

We further analyzed the strain states of YIG and Bi:YIG films via reciprocal space mappings (RSMs) around the (486) diffraction. The representative results obtained from the YIG and Bi:YIG films on GGG(111) and GSGG(111) substrates are shown in Figs. 2(a)–2(d) (the other results are shown in Figs. S3 and S4 in the supplementary materials). In all of the RSMs, the (486) diffractions of the YIG and Bi:YIG films share the same in-plane reciprocal vectors with those of the substrates, demonstrating a coherent strain state. In contrast with the Q_x values, the out-of-plane Q_z values of the YIG or Bi:YIG (486) diffractions are quite different from those of the substrates. For the films grown on GSGG(111), the Q_z values of YIG and Bi:YIG are much larger than for films grown on GGG(111), signifying shortened out-of-plane [111] axes. Moreover, because of the doping-induced lattice expansion, the Q_z values for all the Bi:YIG(486) diffractions are smaller than those of the YIG(486) ones. This is also consistent with 2θ–ω XRD linear scans shown in Fig. 1. In Fig. 2(e), the $d_{(111)}$ values for the 30 nm films are plotted as a function of film–substrate lattice mismatch. As the lattice mismatch increases, the $d_{(111)}$ values of both YIG and Bi:YIG films decrease linearly. The $d_{(111)}$ values for 10 nm and 60 nm films are included in Fig. S5 in the supplementary materials. Although these films are also coherently strained, the $d_{(111)}$ values become slightly larger. The reason for such an unexpected lattice expansion is still an open question. We speculate that these lattice expansions may originate from the off-stoichiometry defects accumulated during long-duration deposition or interdiffusion at the film–substrate interface.[30]

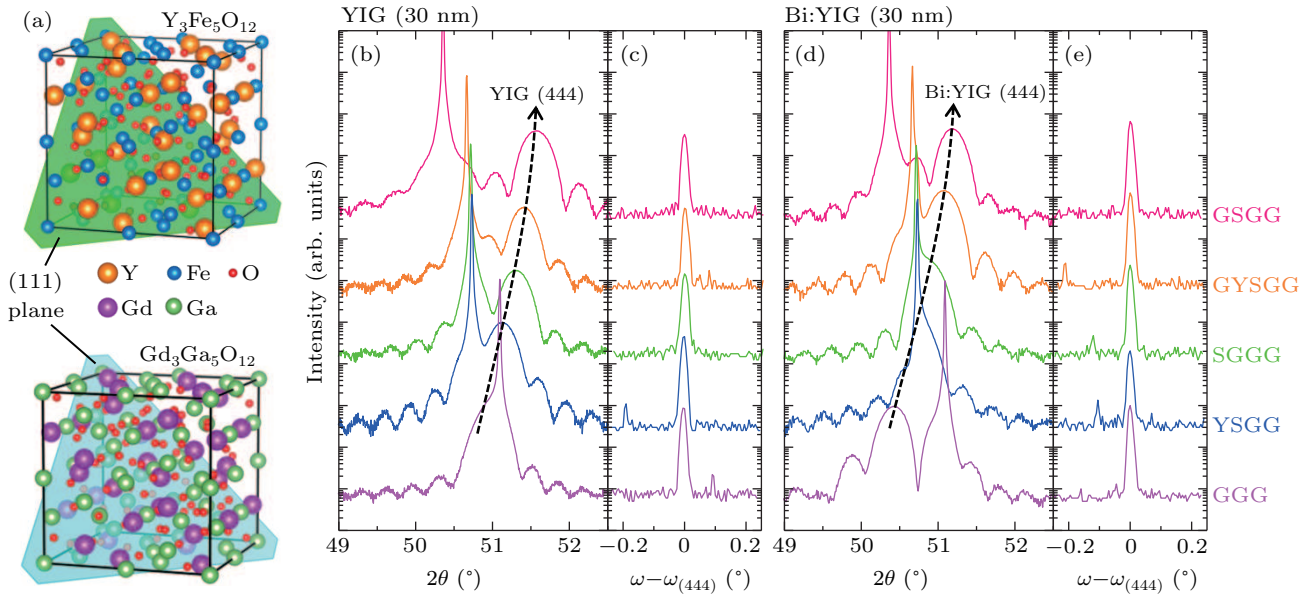


Fig. 1. (a) Schematic crystal structure of YIG (top) and GGG (bottom). The (111) atomic planes are marked in green and cyan. (b), (c) XRD 2θ–ω linear scans (b) and rocking curves (c) near the YIG(444) diffraction from a series of 30 nm thick YIG films on GGG, YSGG, SGGG, GYSGG and GSGG(111) substrates. XRD 2θ–ω linear scans (d) and rocking curves (e) near the Bi:YIG(444) diffraction from a series of 30 nm thick Bi:YIG films on GGG, YSGG, SGGG, GYSGG, and GSGG(111) substrates.

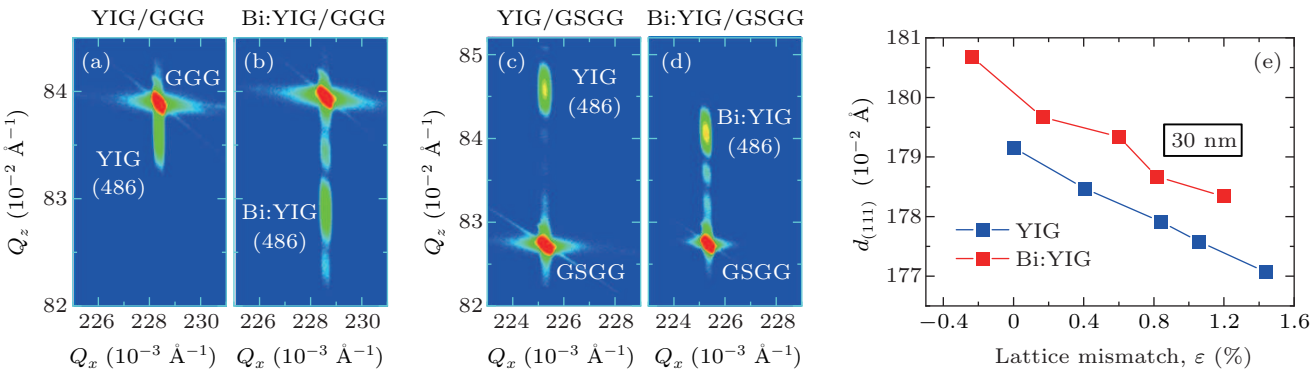


Fig. 2. (a)–(d) High-resolution RSMs around the (486) diffraction of 30 nm YIG and Bi:YIG films grown on GGG(111) and GSGG(111) substrates. (e) The out-of-plane $d_{(111)}$ of 30 nm YIG and Bi:YIG films plotted as a function of lattice mismatch between the film and garnet substrates.

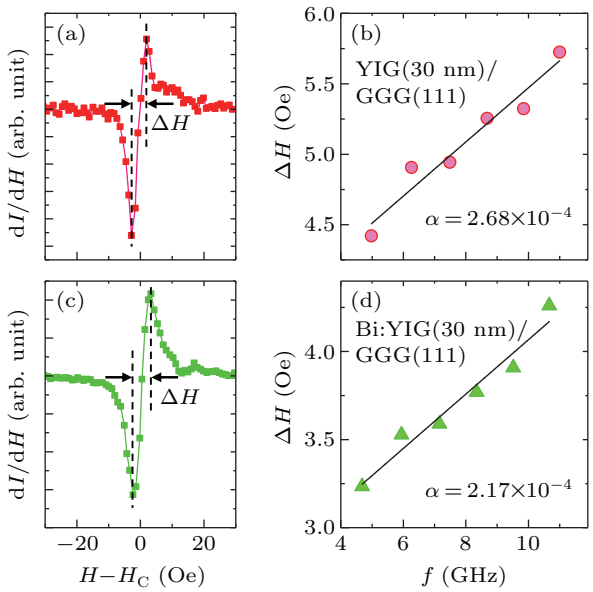


Fig. 3. FMR absorption spectra of 30 nm thick YIG/GGG(111) (a) and Bi:YIG/GGG(111) (c) films under 10 GHz. The absorption line width is marked by dashed lines. Frequency dependent FMR linewidth of YIG/GGG(111) (b) and Bi:YIG/GGG(111) (d). The linear fits are plotted with black lines. The calculated damping constant α is also inserted in (b) and (d).

Low magnetic loss is not only the key advantage of YIG but is also an important fingerprint of film quality. Based on this consideration, we selected the 30 nm thick YIG/GGG(111) and Bi:YIG/GGG(111) films to characterize the Gilbert damping constant by FMR measurements. We scanned the static magnetic field (H) and measured the absorption spectrum of microwaves at a specific frequency (f). The line width (ΔH) of the FMR absorption spectrum can be obtained by Lorentz fitting. Figures 3(a) and 3(c) show the representative FMR absorption spectra of 30 nm thick YIG/GGG(111) and Bi:YIG/GGG(111) films at $f = 10$ GHz. Figures 3(b) and 3(d) show a set of ΔH values obtained by measuring the FMR absorption spectra at different f ranging from 4 GHz to 11 GHz. The ΔH–f curve can be linearly fitted by

$$\Delta H = \Delta H_0 + \frac{2\alpha}{\gamma} f,$$

where ΔH is the intercept, α is the damping constant and γ is the gyromagnetic ratio. The γ value can be obtained from the Kittel formula

$$f = \gamma \sqrt{H_{\mathrm{FMR}} \left(H_{\mathrm{FMR}} + 4\pi M_{\mathrm{eff}}\right)},$$

where H_{FMR} is the ferromagnetic resonance magnetic field and M_{eff} is the effective magnetization. As inserted in Figs. 3(b) and 3(d), the calculated α values for YIG and Bi:YIG films are 2.6799×10^{-4} and 2.1714×10^{-4}, which are comparable to or lower than most of the YIG films grown by PLD.[31] The fitting results of the Kittel formula are given in Fig. S6 in the supplementary materials. The low magnetic damping once again manifests the high quality of our films.[32] Our results therefore further confirm that Bi doping does not cause a detectable increment in the magnetic loss.

After confirming the high quality of YIG and Bi:YIG films with both structural and FMR characterization, we turned to investigate their static magnetic properties. Figure 4 shows the H-dependent magnetization (M–H) hysteresis loops of the 30 nm thick YIG and Bi:YIG films grown on various garnet substrates. The zoomed-in M–H loops near the zero-field ranges are included in Fig. S9 in the supplementary materials, which clearly presents the detailed coercive field and remnant magnetization. The M–H hysteresis loops of 10 nm and 60 nm thick YIG and Bi:YIG films are included in Figs. S7 and S8 in the supplementary materials. The diamagnetic or paramagnetic backgrounds from the substrates had already been subtracted by linear fitting of the saturated regions in the loops. The M–H curves were measured with H parallel or perpendicular to the film surface, denoted as $H_{\parallel}$ and $H_{\perp}$, respectively, and the M values were normalized by the saturated magnetization (M_{S}) for clarity.

The M–H curves exhibit strong dependence on the epitaxial strain. For the 30 nm thick YIG/GGG(111) films (Fig. 4(a)), the saturation field (H_{S}) in the $H_{\parallel}$ case (about 3 Oe) is much smaller than that in the $H_{\perp}$ case ($\sim$ 2200 Oe). Namely, the YIG/GGG(111) film shows a magnetic easy plane (MEP) behavior. For the YIG films grown on YSGG(111), SGGG(111), and GYSGG(111) substrates (Figs. 4(b)–4(d)), the MEP behavior persists, and H_{S} in the $H_{\perp}$ case decreases gradually as a_{sub} increases. For the YIG/GSGG(111) film, by contrast, H_{S} in the $H_{\parallel}$ case turns out to be larger than that in the $H_{\perp}$ case, which strongly suggests a uniaxial PMA. As marked in Fig. 4, the anisotropic field H_{A} is H_{S} along the magnetic hard axis, and we define the H_{A} value to be positive (negative) in the MEP (PMA) case. Such an evolution from MEP to PMA was also observed in the Bi:YIG films (Figs. 4(f)–4(j)). Compared with the YIG films, H_{A} of the Bi:YIG films in the MEP case show a clear reduction, and the transition from MEP to PMA appears in the Bi:YIG/SGGG(111) films. Namely, Bi-doping can assist the tensile strain and facilitate PMA.

Now we turn to discuss the origin of MA in the YIG and Bi:YIG films. Given a YIG film, MA is contributed to by intrinsic magnetocrystalline MA in the cubic symmetry, the strain-related magnetoelastic effect and shape-related demagnetization effects. Hence the effective MA energy (K_{eff}) can be represented by the following equation:

$$K_{\mathrm{eff}} = K_{\mathrm{shap}} + K_{\mathrm{strain}} + K_{\mathrm{cryst}},$$

where K_{cryst}, K_{strain}, and K_{shap} are the MA energy terms of intrinsic magnetocrystalline anisotropy, strain-induced magnetocrystalline anisotropy and shape anisotropy,

respectively.[33,34] $K_{\rm eff}$ can be determined experimentally by

$$K_{\rm eff} = \frac{H_{\rm A} \cdot M_{\rm s}}{2},$$

and $K_{\rm shap}$ for thin films can be determined experimentally by

$$K_{\rm shap} = 2\pi M_{\rm S}^2 \cos^2\theta,$$

where θ is the angle between the magnetic moment and the film plane. As H aligns along the film normal, the above equation becomes $K_{\rm shap} = 2\pi M_{\rm S}^2$.

According to previous literature, the intrinsic magnetocrystalline anisotropy $K_{\rm cryst}$ of bulk YIG is at least one order of magnitude smaller than $K_{\rm shap}$ and $K_{\rm strain}$.[21,35] Namely, the main contribution to the magnetocrystalline anisotropy of YIG films comes from the epitaxial strain-mediated magnetoelastic effect. On this basis, we rewrite $K_{\rm cryst} + K_{\rm strain}$ as $K_{\rm lattice}$, denoting the MA related to the film lattice. By subtracting $K_{\rm shap}$ from $K_{\rm eff}$, we can determine the $K_{\rm lattice}$ term from all the YIG and Bi:YIG samples.

To explore the relationship between epitaxial strain and magnetocrystalline anisotropy, we calculated the $K_{\rm lattice}$ values of YIG and Bi:YIG films. Based on the definition of $H_{\rm A}$, a positive $K_{\rm lattice}$ tends to align the magnetic moment in-plane while a negative $K_{\rm lattice}$ tends to align the magnetic moment along the film normal. According to the structural characterizations, the lattice distortions of these films are not only dependent on the lattice mismatch ε but also on the film thickness. Based on this consideration, in Fig. 5 we plot $K_{\rm lattice}$ as a function of the out-of-plane lattice constant $d_{(111)}$. Both the YIG and the Bi:YIG films show a linear relationship between $K_{\rm lattice}$ and $d_{(111)}$. The slopes of the $K_{\rm lattice}$–$d_{(111)}$ curves exhibit a weak dependence on film thickness. For the 10 nm and 60 nm films with a slightly larger $d_{(111)}$, the slope is consistent with the thinner films. Therefore, the key control parameter for the strain-induced MA should not be the nominal substrate–film lattice mismatch ε but the rhombohedral lattice distortion along the out-of-plane (111) axis. For the films grown on a GGG(111) substrate with a relatively small $a_{\rm sub}$, the compressive strain tends to elongate $d_{(111)}$ and induce a positive $K_{\rm lattice}$, which works cooperatively with $K_{\rm shap}$ and results in clear MEP behavior. For those films grown on other garnet substrates with larger $a_{\rm sub}$, the strain states evolve from compressive to tensile, and the resultant negative $K_{\rm lattice}$ can compete with and eventually overwhelm $K_{\rm shap}$, leading to PMA. More interestingly, the strain-induced magnetocrystalline anisotropies for YIG and Bi:YIG films are very different. As $d_{(111)}$ decreases, the negative $K_{\rm lattice}$ of Bi:YIG films increases much faster than that of the YIG films. In other words, the epitaxial strain-induced lattice distortion can be more effective in enhancing the PMA.

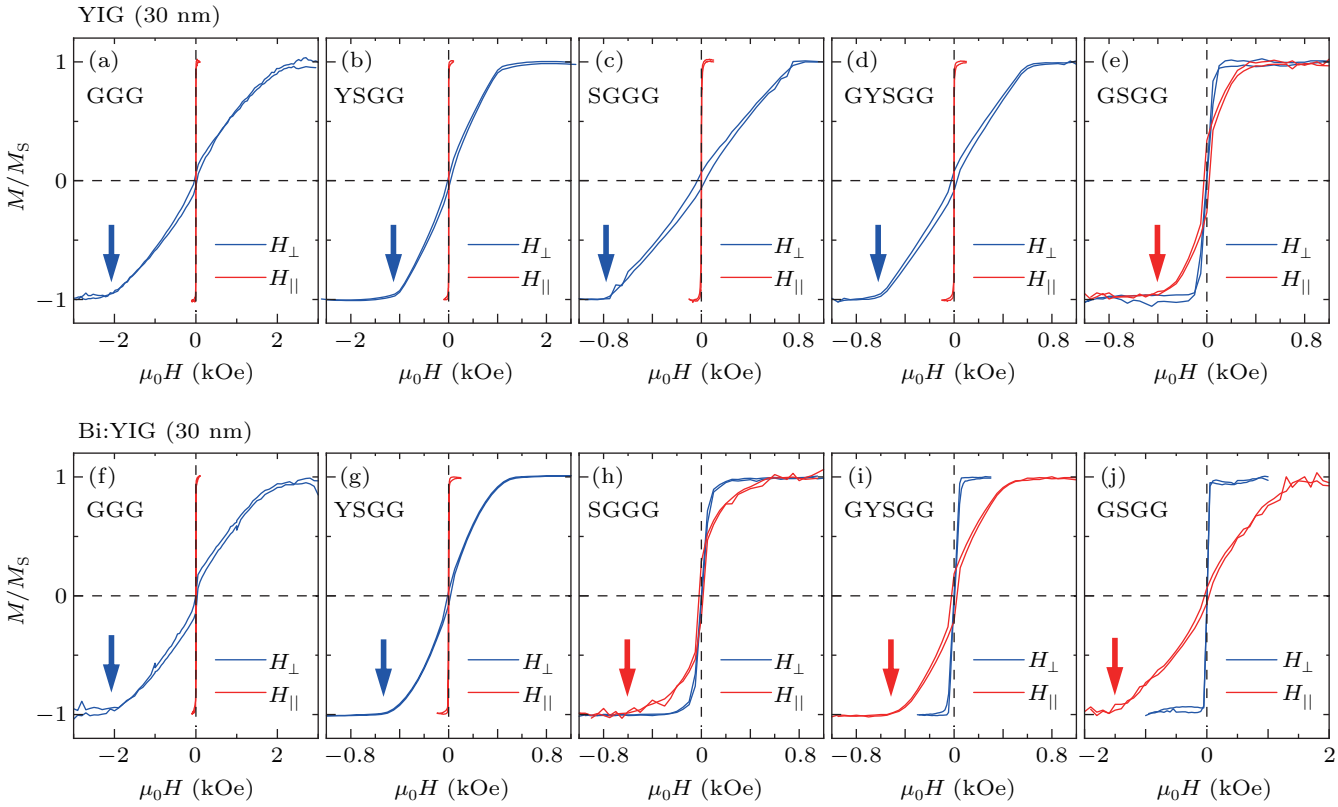


Fig. 4. (a)–(e) M–H hysteresis loops measured at 300 K for the 30 nm thick YIG films on various garnet substrates with H parallel to the in-plane ($H_{\parallel}$) and out-of-plane ($H_{\perp}$) directions. (f)–(j) M–H hysteresis loops measured at 300 K for the 30 nm thick Bi:YIG films on various garnet substrates with H parallel to the in-plane ($H_{\parallel}$) and out-of-plane ($H_{\perp}$) directions. The magnetic anisotropic field $H_{\rm A}$ is marked by solid arrows.

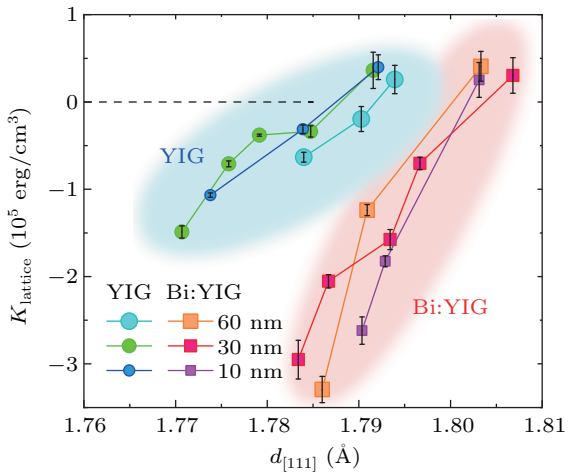


Fig. 5. The out-of-plane lattice constant $d_{[111]}$ dependent magnetocrystalline anisotropy K_{lattice} of YIG and Bi:YIG epitaxial films for various film thicknesses.

Now we turn to discuss the origin of the strain and doping modulations of MA in YIG films. The epitaxial strain and chemical doping usually affect MA through charge transfer or structural modulations.[36–38] Note that the YIG films and garnet substrates are highly insulating, and Bi is an isovalent dopant in Bi:YIG. Based on these facts, we suggest that charge transfer should not occur either inside the YIG films or at the YIG–GGG interfaces. Thus, strain-induced structural modulation should be the main cause of MA modulation. Although the (111)-oriented garnet substrates share the same cubic symmetry with the YIG and Bi:YIG films, the three-fold constraints in the (111) plane can impose rhombohedral distortions in the YIG and Bi:YIG films. The cubic lattice will be elongated along the out-of-plane [111] axis, and considerable ionic displacement could occur inside YIG unit cells. Such ionic displacements can change interatomic distances and alter MA through spin–orbit coupling.[34] According to previous works, the magnetoelastic coefficient along the [111] axis for YIG is negative.[21–23] Hence, it is expected that the in-plane tensile strain-induced compression of $d_{(111)}$ facilitates PMA, while the compressive strain-induced elongation of $d_{(111)}$ facilitates MEP. This is consistent with our observations. The Bi doping can further modulate this strain-induced MA. On one hand, the Y^{3+} and heavy Bi^{3+} doping may lead to cation ordering and provide additional local symmetry breaking of the FeO_4 tetrahedron,[39] which may further magnify the magnetoelastic effect. On the other hand, the Bi^{3+} cations with larger spin–orbit coupling can alter the superexchange interactions and single-ion anisotropy of local spins in Fe^{3+} cations.[40] Thanks to these two effects, although the lattice mismatches between Bi:YIG and substrates are smaller than those of the YIG films, the strain-induced magnetocrystalline anisotropy of Bi:YIG films is much stronger. Namely, Bi doping can magnify the strain-mediated MA of epitaxial YIG films.

4. Summary

In conclusion, we utilized high-quality YIG and Bi:YIG epitaxial films as model systems to investigate the collective effects of epitaxial strain and chemical doping on MA. We found that the tensile (compressive) strain imposed by the substrate facilitates PMA (MEP). The key parameter that determines strain-mediated MA is the rhombohedral-like out-of-plane lattice distortion. Bi doping plays an important role in enhancing the tunability of strain-mediated MA. Namely, it is much easier to induce prominent PMA by epitaxial tensile strain in Bi:YIG films. Moreover, ultra-low magnetic damping persists in these heavily Bi-doped YIG films. Our work provides guidelines for effectively harnessing MA in garnet-type ferrite films, which is essential for practically applying these systems in spintronic devices.

Acknowledgments

Project supported by the National Basic Research Program of China (Grant No. 2020YFA0309100), the National Natural Science Foundation of China (Grant Nos. 12074365 and U2032218), the Fundamental Research Funds for the Central Universities (Grant Nos. WK9990000108, WK9990000102, and WK2030000035), and Hefei Science Center CAS Foundation (Grant No. 2021HSC-UE010). The sample fabrication was partially carried out at the USTC Center for Micro and Nanoscale Research and Fabrication and the magnetic characterizations were carried out in the Instruments Center for Physical Science, USTC.

References

[1] Sozeri H and Ghazanfari N 2009 *J. Phys.: Conf. Ser.* **153** 12066
[2] Kurebayashi H, Dzyapko O, Demidov V E, Fang D, Ferguson A J and Demokritov S O 2011 *Nat. Mater.* **10** 660
[3] Schmidt G, Hauser C, Trempler P, Paleschke M and Papaioannou E T 2020 *Phys. Status Solidi B* **257** 1900644
[4] Kato Y K, Myers R C, Gossard A C and Awschalom D D 2004 *Science* **306** 1910
[5] Hahn C, de Loubens G, Viret M, Klein O, Naletov V V and Ben Youssef J 2013 *Phys. Rev. Lett.* **111** 217204
[6] Qu D, Huang S Y, Miao B F, Huang S X and Chien C L 2014 *Phys. Rev. B* **89** 140407
[7] Cai K, Yang M, Ju H, Wang S, Ji Y, Li B, Edmonds K W, Sheng Y, Zhang B, Zhang N, Liu S, Zheng H and Wang K 2017 *Nat. Mater.* **16** 712
[8] Schreier M, Chiba T, Niedermayr A, Lotze J, Huebl H, Geprägs S, Takahashi S, Bauer G E W, Gross R and Goennenwein S T B 2015 *Phys. Rev. B* **92** 144411
[9] Giles B L, Yang Z, Jamison J S, Gomez-Perez J M, Vélez S, Hueso L E, Casanova F and Myers R C 2017 *Phys. Rev. B* **96** 180412
[10] Avci C O, Quindeau A, Pai C, Mann M, Caretta L, Tang A S, Onbasli M C, Ross C A and Beach G S D 2017 *Nat. Mater.* **16** 309
[11] Nakayama H, Althammer M, Chen Y T, Uchida K, Kajiwara Y, Kikuchi D, Ohtani T, Geprägs S, Opel M, Takahashi S, Gross R, Bauer G E W, Goennenwein S T B and Saitoh E 2013 *Phys. Rev. Lett.* **110** 206601
[12] D'Allivy Kelly O, Anane A, Bernard R, Ben Youssef J, Hahn C, Molpeceres A H, Carrétéro C, Jacquet E, Deranlot C, Bortolotti P, Lebourgeois R, Mage J C, de Loubens G, Klein O, Cros V and Fert A 2013 *Appl. Phys. Lett.* **103** 82408

[13] Heinrich B, Burrowes C, Montoya E, Kardasz B, Girt E, Song Y, Sun Y and Wu M 2011 *Phys. Rev. Lett.* **107** 066604

[14] Bauer G E W, Saitoh E and van Wees B J 2012 *Nat. Mater.* **11** 391

[15] Sbiaa R, Meng H and Piramanayagam S N 2011 *Phys. Status Solidi-R* **5** 413

[16] Wei W, Wang H, Zhang K, Liu H, Kou Y, Chen J, Du K, Zhu Y, Hou D, Wu R, Yin L and Shen J 2015 *Chin. Phys. Lett.* **32** 87504

[17] Wang H, Song J, Wang W, Chen Y, Shen X, Yao Y, Li J, Sun J and Yu R 2021 *Chin. Phys. Lett.* **38** 87502

[18] Chen S, Xie Y, Yang Y, Gao D, Liu D, Qin L, Yan W, Tan B, Chen Q, Gong T, Li E, Bi L, Liu T and Deng L 2022 *Chin. Phys. B* **31** 048503

[19] Zhang Y, Yang Q, Liu X, Zhang D, Rao Y and Zhang H 2021 *AIP Adv.* **11** 65113

[20] Kubota M, Tsukazaki A, Kagawa F, Shibuya K, Tokunaga Y, Kawasaki M and Tokura Y 2012 *Appl. Phys. Express* **5** 103002

[21] Fu J, Hua M, Wen X, Xue M, Ding S, Wang M, Yu P, Liu S, Han J, Wang C, Du H, Yang Y and Yang J 2017 *Appl. Phys. Lett.* **110** 202403

[22] Ding J, Liu C, Zhang Y, Erugu U, Quan Z, Yu R, McCollum E, Mo S, Yang S, Ding H, Xu X, Tang J, Yang X and Wu M 2020 *Phys. Rev. Appl.* **14** 014017

[23] Li G, Bai H, Su J, Zhu Z Z, Zhang Y and Cai J W 2019 *APL Mater.* **7** 41104

[24] Liu X, Yang Q, Zhang D, Wu Y and Zhang H 2019 *AIP Adv.* **9** 115001

[25] Soumah L, Beaulieu N, Qassym L, Carrétéro C, Jacquet E, Lebourgeois R, Ben Youssef J, Bortolotti P, Cros V and Anane A 2018 *Nat. Commun.* **9** 3355

[26] Chen J, Wang C, Liu C, Tu S, Bi L and Yu H 2019 *Appl. Phys. Lett.* **114** 212401

[27] Wang C T, Liang X F, Zhang Y, Liang X, Zhu Y P, Qin J, Gao Y, Peng B, Sun N X and Bi L 2017 *Phys. Rev. B* **96** 224403

[28] Kehlberger A, Richter K, Onbasli M C, Jakob G, Kim D H, Goto T, Ross C A, Götz G, Reiss G, Kuschel T and Kläui M 2015 *Phys. Rev. Appl.* **4** 014008

[29] Chang H 2017 *Nanometer-thick Yttrium Iron Garnet Film Development and Spintronics-related Study* (Ph.D. Dissertation) (Fort Collins: Colorado State University)

[30] Suturin S M, Korovin A M, Bursian V E, Lutsev L V, Bourobina V, Yakovlev N L, Montecchi M, Pasquali L, Ukleev V, Vorobiev A, Devishvili A and Sokolov N S 2018 *Phys. Rev. Mater.* **2** 104404

[31] Onbasli M C, Kehlberger A, Kim D H, Jakob G, Kläui M, Chumak A V, Hillebrands B and Ross C A 2014 *APL Mater.* **2** 106102

[32] Sparks M 1964 *Ferromagnetic Relaxation Theory* (New York: McGraw Hill) p. 160

[33] Coey J M D 2009 *Magnetism and Magnetic Materials* (New York:Cambridge University Press) p. 168

[34] Wang H, Du C, Hammel P C and Yang F 2014 *Phys. Rev. B* **89** 134404

[35] Von Aulock W H 1965 *Handbook of Microwave Ferrite Materials* (London: Academic Press)

[36] Feng C, Wang S, Yin L, Li X, Yao M, Yang F, Tang X, Wang L, Mi W and Yu G 2018 *Adv. Funct. Mater.* **28** 1803335

[37] Wang L, Feng C, Li Y, Meng F, Wang S, Yao M, Xu X, Yang F, Li B and Yu G 2019 *ACS Appl. Mater. Inter.* **11** 32475

[38] Vasili H B, Casals B, Cichelero R, Macià F, Geshev J, Gargiani P, Valvidares M, Herrero-Martin J, Pellegrin E, Fontcuberta J and Herranz G 2017 *Phys. Rev. B* **96** 014433

[39] Akselrad A and Callen H 1971 *Appl. Phys. Lett.* **19** 464

[40] Hansen P and Witter K 1985 *J. Appl. Phys.* **58** 454